Hypersonic Aerothermoelastic Response Prediction of Skin Panels Using Computational Fluid Dynamic Surrogates

Andrew R. Crowell[1,4]
Jack J. McNamara[2,4]
Brent A. Miller[3,4]

Abstract

Computational Fluid Dynamic (CFD) surrogates are developed to efficiently compute the aerodynamic heating and unsteady pressure loads for a structurally and thermally compliant skin panel in hypersonic flow. In order to minimize the computational overhead, the surrogates are constructed using steady-state CFD flow analysis. Unsteady terms in the aerodynamic pressure are incorporated using piston theory. The surrogates are compared to both analytical modeling (i.e., piston theory and Eckerts methods) and Reynolds Averaged Navier-Stokes CFD predictions of the aerothermodynamic loads for representative panel responses. Results indicate that the surrogates accurately and efficiently reproduce CFD predictions for the aerothermodynamic loads. Comparisons of the dynamic aerothermoelastic panel response using the surrogates with previous results using analytical approaches reveal differences of over 100% in the onset time to flutter, and significantly altered post-flutter responses. The CFD surrogates are found to enable a reasonably accurate, robust, and efficient method for incorporating CFD loads prediction, which would otherwise be impractical, into a long time-record aerothermoelastic analysis of structures for a complete hypersonic trajectory.

1. Introduction

Currently, there is a strong desire for responsive hypersonic cruise vehicles and improved access to space using next generation air breathing technologies. However, modeling and analysis of this class of vehicle is challenging due to inherent structural flexibility, extended operation within the atmosphere at high Mach numbers, and the use of fully integrated air-breathing propulsion systems. These characteristics result in severe structural loads, path dependence of structural properties on operating conditions, and significant coupling between the aerodynamic, propulsion, structural, and control systems. Specifically, aerothermoelastic interactions, which are mutually coupled interactions between the aerothermal and structural dynamics of a system, are an important concern for hypersonic vehicles, impacting: materials selection, structural analysis/design/life forecasting, aero-propulsion integration, thermal management, and controller design.

The need to account for aerothermoelastic interactions, combined with the path dependence of structural properties on operating conditions, indicates that a multi-physics analysis of a hypersonic configuration may need to be carried out over relatively long portions of a trajectory. The impracticality of using ground-based experimental testing[5, 12] to meet this need implies that computational simulation will have the primary role in such an analysis. These issues, among others, have led to a United States Air Force funded research project by Boeing and Lockheed Martin to revisit design practices of hypersonic vehicles[26, 49].

---

[1] Ph.D. Candidate
[2] Assistant Professor
[3] Graduate Research Assistant
[4] Department of Mechanical & Aerospace Engineering, Ohio State University, Columbus, OH, 43210, USA

Performing a long time-record numerical multi-physics analysis is an arduous task considering the high computational cost and the potential need to account for substantial uncertainty in hypersonic aerothermodynamic predictions[5, 6] using non-deterministic techniques[23]. These two issues strictly limit the formulation of a multi-physics model to methods that are computationally efficient. This constraint combined with the complexity of the flow physics in the hypersonic environment makes accurate modeling of the flow induced structural loads an important concern. Historically, the hypersonic aerothermodynamic loads have been approximated using either computational fluid dynamic (CFD) solutions to the Navier-Stokes equations, or basic analytical approaches. CFD relies on the fewest assumptions, and provides the potential to capture the complete flow physics. However, the associated computational expense makes trajectory scale and/or probabilistic analysis intractable for a multi-physics analysis. At the other end of the modeling spectrum, analytical approaches provide efficient prediction of the aerodynamic pressure and heating, albeit at the expense of several simplifying assumptions[7, 30].

The disadvantages of both CFD and analytical approaches have motivated the development of reduced-order models (ROMs), which seek to provide an accurate description of a system at a computational cost that is a fraction of that needed for a high-fidelity analysis. Typical approaches for constructing ROMs for unsteady, nonlinear flows are proper orthogonal decomposition (POD)[11, 17, 29], Volterra series[29, 42], and surrogates[14, 15, 30, 43, 46]. Each of these seek to identify the primary features of a system from a limited number of high-fidelity flow solutions. The generation of this dataset requires an initial computational investment. However, this process is efficiently carried out using parallel computing facilities. POD represents a spectral method, where an orthogonal modal basis is computed from snapshots of the full-order system response to relevant inputs[29]. The Volterra series method uses the assumption that the response of any nonlinear system is exactly represented by an infinite series expansion of multidimensional convolution integrals of Volterra kernals. A Volterra series ROM is constructed by computing a truncated set of kernals from the full-order system response to a set of known inputs[29]. Surrogate based approaches identify a continuous approximate function, i.e., "surrogate function" from a discrete sampling of an unknown, nonlinear function over a bounded set of inputs[37]. Methods for constructing the surrogate function include radial basis functions, neural networks, polynomial response surfaces, and kriging[15, 37].

Despite extensive research into aerodynamic ROMs[29], only a limited number of studies are relevant to hypersonic flow. Lucia[28] examined POD to model aerodynamic systems with strong shocks and nonlinearity in the parameter space. Tang et al.[44] developed a POD based ROM for predicting steady-state pressure and temperature distributions on the surface of a rigid hypersonic vehicle resembling the X-34. These studies found that a POD based ROM is suitable for accurate representation of high speed flows with shocks and nonlinearity in the parameter space.

Recent work[30] has investigated kriging surrogates for modeling static force coefficients as a function of arbitrary airfoil motions of a two degree-of-freedom typical-section in hypersonic flow. Kriging was used since the method is well-suited to approximating nonlinear functions and does not require *a priori* assumptions on the form of the function that is to be approximated[37]. The kriging surrogates provided excellent agreement with CFD solutions to the Navier-Stokes equations, while requiring less than one thousandth of a second to compute the lift and moment coefficients. In a related study[14], a kriging surrogate was constructed to compute the steady-state aerodynamic heat loads over a three-dimensional control surface, and subsequently used in a broader reduced-order aerothermoelastic analysis.

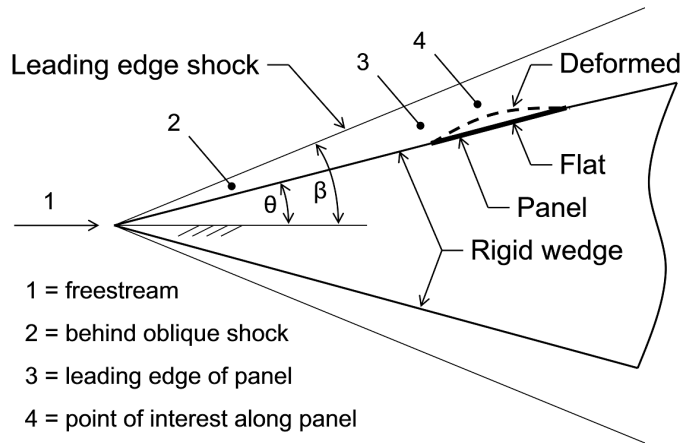Results from [30] and [14], as well as similar work done in lower Mach number

Figure 1: Panel located on an inclined surface of a wedge-shaped forebody [7].

regimes[15, 16, 43, 46], illustrate that surrogate based approaches are promising for accurate and efficient modeling of complex fluid dynamic phenomena. The goals of this study are to further examine surrogate based approaches for use in hypersonic aerothermoelasticity, and also to investigate the importance of CFD-based aerothermodynamic loads on the aerothermoelastic response of skin panels in hypersonic flow. The specific objectives are:

1. Compare and quantify the differences between analytical, CFD, and surrogate approaches for predicting aerodynamic heat and pressure loads on compliant skin panels;

2. Perform a long time record (~30 minutes) dynamic aerothermoelastic analysis of a skin panel in hypersonic flow using CFD surrogates, and highlight differences in aerothermoelastic behavior of skin panels resulting from improved aerothermodynamic modeling;

3. Assess the computational requirements of a dynamic aerothermoelastic analysis using CFD surrogates relative to both an actual CFD analysis and basic analytical approaches.

Fulfilling these objectives provides an important step towards the development of tractable multi-physics simulation frameworks for design and analysis of hypersonic configurations. Since the focus of this paper is on the use of CFD surrogates for aerothermoelastic analysis of skin panels, a basic thermo-elastic model developed by Culler and McNamara[7] is used. This model is based on a Galerkin solution to the cylindrical bending of a 2-D von Kármán panel and a finite difference solution to the 2-D heat equation. An additional advantage to using this model is that results generated by Culler and McNamara[7] using basic aerothermodynamic models serve as a convenient comparison case for the present study.

As shown in Fig. 1, the panel of interest is assumed to be located on the surface of a representative 2-D forebody of a hypersonic cruise vehicle[7]. The panel is assumed fixed with immovable, simple supports. Furthermore, arbitrary, non-uniform, in-plane and through-thickness thermal loads are considered; as well as chord-wise variation of elastic modulus and thermal expansion coefficient with temperature. The operating conditions and panel geometry used in this study are identical to [7] and are listed in Table 1.

The remainder of this paper is constructed as follows. Sections II details the surrogate modeling approach as well as the CFD model used to generate sample/evaluation data. Section III provides a comparison of the CFD surrogates with both standard CFD and simple analytical approaches such as third-order piston theory aerodynamics[25] and Eckert's reference methods for aerodynamic

Table 1: Parameters used in the aerothermoelastic model.

Altitude	30 km
Forebody Surface Inclination, θ	5.0°
Transition to Turbulence Upstream of Panel	1.0 m
Panel Length, a	1.5 m
Plate Thickness, h	5.0 mm

heating[13]. Sections IV and V detail the aerothermoelastic analysis of a skin panel using the developed CFD surrogate.

2.   Aerothermodynamic Analysis Using CFD Surrogates

2.1   Surrogate Based Analysis

As indicated previously, the goal of surrogate based analysis is to identify a computationally efficient "surrogate function" using a limited number of sample points of a complex nonlinear function that is expensive to compute (e.g., Navier-Stokes equations)[37]. Typical surrogate prediction times are on the order of a fraction of a second[15], whereas standard CFD solutions require on the order of minutes to hours. Thus, the benefit of surrogate modeling arises when the cost of the initial sampling is less than the cost of introducing the actual model into the analysis. In the context of hypersonic aerothermoelasticity, the loads may need to be updated thousands of times a second over time spans of minutes[7, 8]. Furthermore, a significant amount of uncertainty is currently associated (and will be for the foreseeable future) with CFD aerothermodynamic predictions[5, 6]. Thus, surrogates enable the implementation of nondeterministic approaches with fluid-thermal-structural analysis over time-records that span several minutes. Kriging is chosen for the present study since it provides the means for non-linear interpolation, it does not require *a priori* assumptions on the form of the actual model, and has demonstrated excellent accuracy for constructing CFD surrogates in hypersonic flow[14, 30]. The process used to construct a Kriging based surrogate is outlined below.

1. Identify a parameter space of interest, i.e. Mach number, structural displacement, surface temperature, etc. Note, time is not considered as a parameter, but is inherently included through changing structural displacements and surface temperatures. This form of parameterization allows for a single surrogate to cover a number of different possible time-dependent trajectories.

2. Generate training sample points from the parameter space. In this study the Latin Hypercube Sampling script LHSDesign in Matlab® is used to pick the training points since it provides a random, yet uniformly distributed sampling of the selected parameter space. The criterion to maximize the minimum distance between sample points is implemented over 1000 iterations.

3. Obtain the desired outputs, i.e. pressure and heat flux, from CFD solutions at the training points.

4. Construct the Kriging surrogate using the DACE[27] toolbox to relate the input parameters from the training sample points to the outputs from the CFD code at those points.

A Kriging surrogate is characterized by local deviations, $\mathbf{C}(\mathbf{d}, \mathbf{X})$, from a global approximation, $\mathbf{R}(\mathbf{d}, \mathbf{X})$. A general form of Kriging is shown in Eq. 1[41],

$$\mathbf{y}(\mathbf{d}) = \mathbf{R}(\mathbf{d}, \mathbf{X}) + \mathbf{C}(\mathbf{d}, \mathbf{X}), \tag{1}$$

where $\mathbf{y}(\mathbf{d})$ is the Kriging prediction at a desired point in the parameter space. Note, $\mathbf{d}$ is a vector of input parameters at the desired sample point, and $\mathbf{X}$

is a matrix of input parameters from the initial training sample points. For this study, the Kriging surrogate is computed using the Design and Analysis of Computer Experiments (DACE)[27] toolbox in Matlab®.

Three input parameters for the surrogate are selected for this study: freestream Mach number, surface deformation, and surface temperature. The Mach number is a scalar quantity and is easily incorporated as an input. However, the deformation and surface temperature require parameterization since each is an arbitrary spatial function that will change for each sample point. A straightforward approach is to approximate the surface deformation and temperature as a summation of spatial functions multiplied by a set of corresponding weights. For example, the structural displacement, $w(x)$, of the panel is conveniently represented using free vibration modes, $\Phi_{ref,i}(x)$:

$$w(x) = \eta_1 \Phi_{ref,1}(x) + \ldots + \eta_N \Phi_{ref,N}(x) \tag{2}$$

Thus, the structural displacement field is parameterized using the nondimensional modal amplitudes, $\bar{\eta}_i = \eta_i/h$, where h is the thickness of the plate provided in Table 1. For the surface temperature, $T_s(x)$, a third-order polynomial is choosen as the spatial function. Thus:

$$T_s(x) = T_1 + T_2 x + T_3 x^2 + T_4 x^3 \tag{3}$$

where T_1 through T_4 are the coefficients of the polynomial, that can be curve fit in a least squares sense to any actual temperature distribution that may occur in an aerothermoelastic simulation. Thus, for the selected input parameters, the Kriging input vector, $\mathbf{d}$, and sample point matrix, $\mathbf{X}$, are:

$$\mathbf{d} = \begin{bmatrix} M_1 & \bar{\eta}_1 & \ldots & \bar{\eta}_N & T_1 & \ldots & T_4 \end{bmatrix}^T \tag{4}$$

$$\mathbf{X} = \begin{bmatrix} M_1^{(1)} & \bar{\eta}_1^{(1)} & \ldots & \bar{\eta}_N^{(1)} & T_1^{(1)} & \ldots & T_4^{(1)} \\ \vdots & \vdots & \ddots & \vdots & \vdots & \ddots & \vdots \\ M_1^{(n)} & \bar{\eta}_1^{(n)} & \ldots & \bar{\eta}_N^{(n)} & T_1^{(n)} & \ldots & T_4^{(n)} \end{bmatrix}^T \tag{5}$$

where n represents the number of sample points taken, M_1 is the freestream Mach number at location 1 shown in Fig. 1.

In order to minimize the computational burden of generating the surrogate sample data, it is assumed that the primary features of the flow are captured using a steady-state analysis. Two aspects of the aerothermoelastic behavior of panels make this a reasonable assumption. First, previous work[7] has found that thermo-elastic coupling of skin panels is primarily quasi-static due to disparate time scales between the heat transfer and aeroelastic subsystems. In addition, as discussed previously, results from Ref. [30] indicate that unsteadiness due to surface motion can primarily be captured by augmenting the steady-state CFD coefficient of pressure with unsteady pressure terms extracted from simple analytical models such as piston theory.

Using these assumptions, the sample points for the surrogate are computed from steady-state CFD flow solutions using statically deformed surfaces. Since the thermo-elastic coupling is assumed to be quasi-static, the resulting surrogate for the aerodynamic heating boundary condition, $Q_{aero}(x)$, is complete and is given by:

$$Q_{aero}(x) = c_p U_3 \rho_3 (T_s(x) - T_{0,3}) \, \mathbf{y_{C_H}}(\mathbf{d}) \tag{6}$$

where c_p is the specific heat at constant pressure, U is the velocity, ρ is the density, T_0 is the total temperature, $\mathbf{y_{C_H}}(\mathbf{d})$ is the surrogate prediction of the Stanton number, and subscript $'3'$ indicates a freestream property at the leading edge of the panel, as shown in Fig. 1. For the pressure coefficient, C_p, additional correction terms are required in order to account for unsteady flow. McNamara

et al.[30] previously derived correction terms for unsteady effects using third-order piston theory:

$$C_p(x) = C_{p,vel}(x) + \bar{C}_p(x,t) + \mathbf{y}_{\mathbf{C_p}}(\mathbf{d}) \tag{7}$$

where $\mathbf{y}_{\mathbf{C_p}}(\mathbf{d})$ is the surrogate prediction of the steady state pressure coefficient, and

$$C_{p,vel}(x) = \frac{2}{M_3 U_3}\left(\frac{\partial w}{\partial t}\right) + \frac{\gamma+1}{2U_3^2}\left(\frac{\partial w}{\partial t}\right)^2 + \frac{(\gamma+1)M_3}{6U_3^3}\left(\frac{\partial w}{\partial t}\right)^3 \tag{8}$$

and

$$\begin{aligned}\bar{C}_p(x) = &\frac{\gamma+1}{U_3}\left(\frac{\partial w}{\partial t}\right)\left(\frac{\partial w}{\partial x}\right) + \frac{(\gamma+1)M_3}{2U_3^2}\left(\frac{\partial w}{\partial t}\right)^2\left(\frac{\partial w}{\partial x}\right) \\ &+ \frac{(\gamma+1)M_3}{2U_3}\left(\frac{\partial w}{\partial t}\right)\left(\frac{\partial w}{\partial x}\right)^2\end{aligned} \tag{9}$$

approximate the components of the pressure coefficient due to aerodynamic damping[30]. Here γ is ratio of specific heats. From Eqs. 7 - 9, the aerodynamic pressure, $q_a(x)$, is:

$$q_a(x) = \frac{1}{2}C_p(x)\rho_3 U_3^2 \tag{10}$$

2.2 Computational Fluid Dynamics Analysis

The NASA Langley CFL3D code[4, 22] is used in this study for Navier-Stokes flow analysis. The CFL3D code uses an implicit, finite-volume algorithm based on upwind-biased spatial differencing to solve the Reynolds Averaged Navier-Stokes (RANS) equations. Note that since CFL3D is an ideal gas code, no real gas effects are included in the CFD analysis. Multigrid and mesh-sequencing are available for convergence acceleration. The algorithm, which is based on a cell-centered scheme, uses upwind-differencing based on either flux-vector splitting or flux-difference splitting, and can sharply capture shock waves. The Menter $k-\omega$ SST[32] turbulence model is used in this study for closure of the RANS equations. Note that the applicability of this turbulence model in the hypersonic regime has been verified in [39, 40].

The computational mesh used in this study is shown in Fig. 2. There are a total of 34,600 cells with a maximum y+ value at the wall of 0.65. The upstream surface is modeled in order to match the assumption in [7] that transition to turbulent flow occurs one meter upstream of the leading edge of the panel. A mesh density study of this configuration was carried out relative to a mesh with factor 2 refinement in the chordwise and vertical directions; demonstrating convergence of the lift coefficient within 0.4%, and drag coefficient within 2%. Finally, note that the Hartwich and Agrawal[19] exponential decay mesh deformation scheme is used to accommodate structural deformation in the fluid domain.

3. Comparison of Aerothermodynamic Modeling Approaches

This section describes study on the differences in aerothermoelastic load predictions using analytical, surrogate, and CFD modeling approaches for the aerodynamic heating and pressure. Two different studies are conducted for the aerodynamic heating. First aerodynamic heating predictions of CFD and Eckert's reference methods are compared. Next, a general assessment of the accuracy of the surrogate model relative to CFD over the selected input parameter space. Similarly, three studies are conducted for the aerodynamic pressure. As with the aerodynamic heating, the accuracy of the surrogate model for predicting steady-state pressure is assessed relative to CFD over the parameter space.
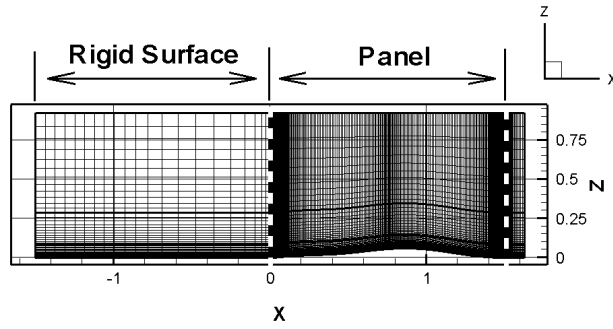
Figure 2: Two-dimensional computational domain of the panel.

7.0	$\leq$	M_1	$\leq$	11.0
-15.00	$\leq$	$\bar{\eta}_1$	$\leq$	15.00
-7.50	$\leq$	$\bar{\eta}_2$	$\leq$	7.50
-3.75	$\leq$	$\bar{\eta}_3$	$\leq$	3.75
-1.90	$\leq$	$\bar{\eta}_4$	$\leq$	1.90
-0.80	$\leq$	$\bar{\eta}_5$	$\leq$	0.80
-0.40	$\leq$	$\bar{\eta}_6$	$\leq$	0.40
300 K	$\leq$	T_1	$\leq$	1800 K
-1000 $\frac{K}{m}$	$\leq$	T_2	$\leq$	1000 $\frac{K}{m}$
-666 $\frac{K}{m^2}$	$\leq$	T_3	$\leq$	666 $\frac{K}{m^2}$
-444 $\frac{K}{m^3}$	$\leq$	T_4	$\leq$	444 $\frac{K}{m^3}$

Table 2: Parameter space used to construct the surrogates.

Second, steady-state aerodynamic pressure predictions of several CFD turbulence models are compared to third-order piston theory for representative panel shapes and surface temperatures at Mach 8.0 and an altitude of 30 km. Finally, predictions of the generalized aerodynamic forces are compared for the surrogate, third-order piston theory, and CFD for a panel vibrating in representative shapes and frequencies.

The selected bounds of the sample parameter space for the surrogate are given in Table 2. These bounds were selected based on previous aerothermoelastic analysis[7] and engineering intuition; with the goal of balancing model generality and the required number of sample points to maintain an accurate model. The maximum amplitude of the panel $|\frac{w}{h}|$ is assumed to ≤ 15. Thus, the first modal amplitude is varied within this range. The amplitude of each higher mode is set ad hoc to half of the previous mode. The temperature profile is assumed to vary to a minimum of 300 K (the initial temperature of the panel) and to a maximum of 1800 K, which exceeds the expected operating condition of the panel for this study[7]. Thus, the bounds of the constant term (T_1) in the surface temperature equation, Eq. 3, are set to these limits. The bounds of the second, third, and fourth temperature coefficients are related to the max temperature difference varying linearly, quadratically, and cubically over the length of the panel, a, defined in Table 1, using:

$$T_{j=2,3,...} = \pm \frac{T_{max} - T_{min}}{a^{j-1}} \quad (11)$$

3.1 Aerodynamic Heating

This section describes study on the differences using analytical, surrogate, and CFD modeling approaches for the aerodynamic heating. First, Eckert's reference methods are described. Next, aerodynamic heating predictions of CFD

and Eckert's reference methods are compared for representative panel shapes and surface temperatures at Mach 8.0 and an altitude of 30 km. Several different turbulence models are included in the CFD flow solutions in order to investigate the uncertainty in aerodynamic heating predictions on deforming skin panels introduced by turbulence modeling. Finally, a general assessment of the accuracy of the surrogate model relative to CFD over the selected input parameter space is performed.

3.1.1   Eckert's Reference Methods

Reference enthalpy methods[13] have been used extensively in approximate analyses to efficiently model convective heating of aerospace vehicles [10, 18, 21, 38, 45, 48]. Eckert's reference enthalpy is given by Eq. (12). The adiabatic wall enthalpy, the total enthalpy, and the recovery factor for turbulent flow are given in Eqs. (13) – (15), respectively [13]. Note that local velocity and enthalpy at the edge of the boundary layer are determined from the local edge Mach number and temperature, respectively.

$$H^* = H_e + 0.50(H_s - H_e) + 0.22(H_{aw} - H_e) \tag{12}$$

$$H_{aw} = r(H_0 - H_e) + H_e \tag{13}$$

$$H_0 = H_e + \frac{U_e^2}{2} \tag{14}$$

$$r = (Pr^*)^{1/3} \tag{15}$$

The Mach number and temperature at the edge of the boundary layer are computed using the local pressure, which is approximated using third-order piston theory aerodynamics [3, 31], combined with isentropic flow relations [1]. Note that this enables feedback of structural deformations to the aerothermal solution. Using flow properties evaluated at the reference enthalpy, the aerodynamic heat flux is computed using Eq. (16). The Stanton number is determined from the Colburn-Reynolds analogy [13, 47] provided in Eq. (17), and the local skin friction coefficient is calculated using the Schultz-Grunow formula [13, 47] given in Eq. (18). The local Reynolds number is defined in Eq. (19) and is computed using the distance from the onset of transition to the point of interest on the panel[47]. Consistent with previous work[7], the leading edge of the panel is assumed to be one meter downstream of the onset of transition. The complete transition from laminar to turbulent flow is assumed to occur within this region, such that flow over the panel is fully turbulent.

$$Q_{aero} = C_H^* \rho^* U_e (H_{aw} - H_s) \tag{16}$$

$$C_H^* = \frac{c_f^*}{2} \frac{1}{(Pr^*)^{2/3}} \tag{17}$$

$$c_f^* = \frac{0.370}{(\log_{10} Re_x^*)^{2.584}} \tag{18}$$

$$Re_x^* = \frac{\rho^* U_e x}{\eta^*} \tag{19}$$

In addition to Eqs. (12) – (19), temperature-enthalpy relations are needed to determine the values of enthalpy at the wall and at the edge of the boundary layer. These relations are also required to determine a temperature from the reference enthalpy in order to evaluate reference density and reference viscosity using the ideal gas law and Sutherland's law, respectively [2]. If the flow is
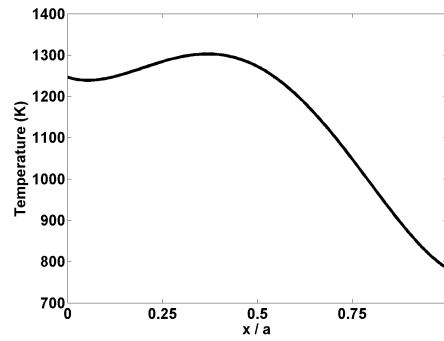
Figure 3:
Representative temperature profile used to compare analytic, surrogate, and CFD aerodynamic heating predictions.

assumed to be calorically perfect, i.e., constant specific heat, then Eq. (20) is used and the reference enthalpy method is equivalent to the reference temperature method [13]. However, since this study is concerned with hypersonic flow, in which the specific heat varies significantly through the boundary layer due to high temperatures and real gas effects [2], temperature-enthalpy tables [20] that include the effect of dissociation based on equilibrium air properties are employed.

$$H = c_p T \tag{20}$$

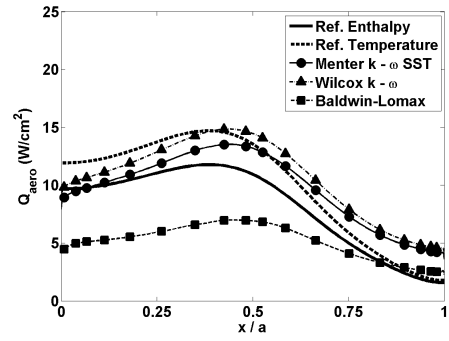### 3.1.2 Comparison of Aerodynamic Heating Modeling Approaches

Bertin and Cummings[5] note that there are several factors affecting the accuracy of CFD modeling of hypersonic vehicles; including: turbulence modeling, transition location, grid density, the ability to model either equilibrium or nonequilibrium flows, and finally correctly modeling vehicle geometry. For the current study, transition location and geometry are prescribed, and the grid density was selected through a convergence study. CFL3D does not consider nonequilibrium flows, however it does have a number of turbulence models available. In another recent study[9], DeBonis *et al* compared different turbulence models and different RANS codes in supersonic flows, and concluded that the dominant factor in the accuracy of the solution was the choice of the turbulence model. Thus, an important consideration for this study is the uncertainty that exists due to different turbulence models. Note, that no experimental data for the operating conditions of this geometry was available for validation. Therefore, aerodynamic heating predictions are compared using: 1) Eckert's reference enthalpy method, 2) Eckert's reference temperature method, 3) RANS with Menter $k - \omega$ SST turbulence model, 4) RANS with Wilcox $k - \omega$ turbulence model, and 5) RANS with Baldwin–Lomax turbulence model.

The surface temperature profile assumed for this comparison is shown in Fig. 3. This profile was computed in Ref. [7] for Mach 8.0 flow after 900 seconds of aerothermoelastic response of the same skin panel considered in this paper. Three different panel deformations are considered. The first, shown in Fig. 4(a), approximates a panel deformation that is influenced by both thermal buckling and aerodynamic pressure in [7]. The second, shown in Fig. 4(c), consists of deformation in the first sine mode and approximates a panel deformation that is primarily driven by thermal buckling in [7]. The third, shown in Fig. 4(e), consists of deformation in the third sine mode, which corresponds to panel deformations during post flutter limit cycle oscillations in [7].

The aerodynamic heating solutions for these deformations are shown in Figs. 4(b,d,f), respectively. In general the spatial distribution of the aerodynamic heat flux is similarly predicted for each approach. However, there is noticable differences at the leading edge of the panel between Eckert's methods and the CFD predictions. This is presumably due to boundary layer displacement effects not modeled by Eckert's methods[7]. Maximum and average differences
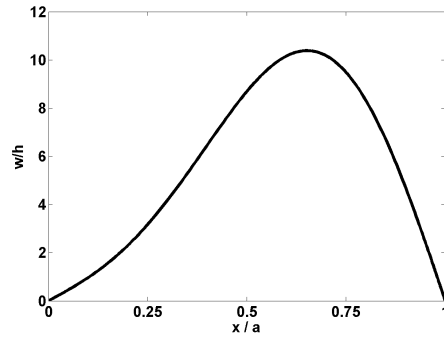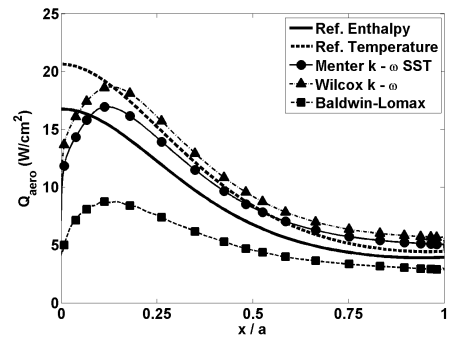
(a) Panel shape 1, ($\bar{\eta}_1 = 8.8187$, $\bar{\eta}_2 = -3.1569, \bar{\eta}_3 = 0.1291$).
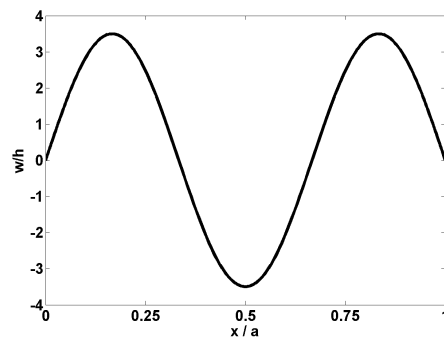
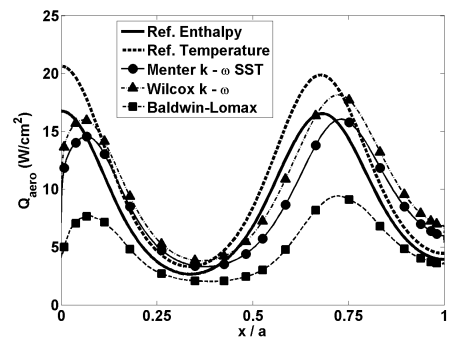(b) Aerodynamic heat flux for panel shape 1.
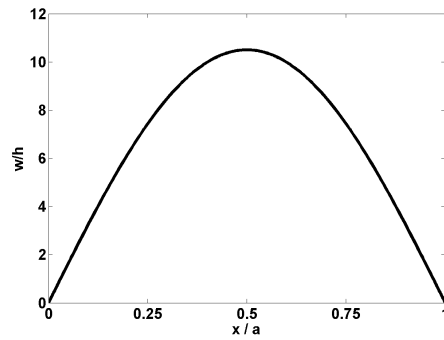
(c) Panel shape 2, ($\bar{\eta}_1 = 10.5$).

(d) Aerodynamic heat flux for panel shape 2.

(e) Panel shape 3, ($\bar{\eta}_3 = 3.5$).

(f) Aerodynamic heat flux for panel shape 3.

Figure 4: Comparison of aerodynamic heating predictions for several panel shapes, $M_1 = 8.0$ at 30 km.

	Ref. Enth. Ref. Temp.	Ref. Enth. Menter	Ref. Temp. Menter
Max.	20.0%	62.2%	95.2%
Avg.	17.3%	21.4%	20.0%

	Wilcox Menter	Baldwin-Lomax Menter	Surrogate Menter
Max.	21.0%	58.7%	3.5%
Avg.	10.6%	44.5%	1.4%

Table 3: Percent difference in aerodynamic heating predictions using different modeling approaches.

T_s 2nd *Order*

300 K	$\leq$	T_1	$\leq$	1800 K
-1000 $\frac{K}{m}$	$\leq$	T_2	$\leq$	1000 $\frac{K}{m}$
-666 $\frac{K}{m^2}$	$\leq$	T_3	$\leq$	666 $\frac{K}{m^2}$

T_s 4th *Order*

300 K	$\leq$	T_1	$\leq$	1800 K
-1000 $\frac{K}{m}$	$\leq$	T_2	$\leq$	1000 $\frac{K}{m}$
-666 $\frac{K}{m^2}$	$\leq$	T_3	$\leq$	666 $\frac{K}{m^2}$
-444 $\frac{K}{m^3}$	$\leq$	T_4	$\leq$	444 $\frac{K}{m^3}$
-296 $\frac{K}{m^4}$	$\leq$	T_5	$\leq$	296 $\frac{K}{m^4}$

Table 4: Parameter space for the 2nd and 4th order temperature profile evaluation cases.

between the different models and the RANS with Menter $k - \omega$ SST turbulence model are provided in Table 3. Maximum differences are as high 95% and average differences are between 10 - 45%. However, the surrogate model (not shown), constructed from 1200 RANS/Menter $k - \omega$ CFD sample points, has a maximum error of 3.5%, and an average error of 1.4%.

Since it was noted earlier that CFL3D is an ideal gas code, it is useful to consider the approximately 20% difference between the reference enthalpy and temperature methods in Table 3. Since the reference temperature method uses an assumption of a calorically perfect gas[7], this difference partially represents the offset in heat flux that could be expected if a real gas model was used in the CFD analysis. However, note that this variation is within the maximum variation found by simply using different turbulence models. Thus, while using an ideal gas assumption introduces error into the present analysis, it is expected to be within the standard bounds of uncertainty for computational aerothermodynamic predictions of RANS CFD codes.

3.1.3 Assessment of Surrogate Accuracy for Aerodynamic Heating

In order to characterize expected accuracy, surrogates constructed from 100, 400, 800, and 1200 sample points are compared to three different sets of 500 CFD solutions. These sets of evaluation cases are computed at points in the input parameter space different than those sampled to construct the surrogates. Each set of 500 CFD evaluation cases corresponds to a second, third, or fourth order polynomial distribution of surface temperature. The three different surface temperature polynomials are used in order to assess the robustness of the surrogate for temperature distributions that do not exactly fit the third order polynomial distribution used to construct the surrogate. For the second and fourth order surface temperature profile evaluation cases, the surrogate temperature coefficients given in Eq. 3 are fit to the second and fourth order temperature profiles in a least squares sense. The bounds of the temperature coefficients for the two sets of evaluation cases with different temperature profiles are shown in Table 4.

In order to quantify the expected accuracy, the normalized root mean square error (NRMSE) is computed as:

$$\text{NRMSE}^{(j)}(\%) = \frac{\sqrt{\frac{1}{p}\sum_{i=1}^{p}\left(\text{Surrogate}_{i}^{(j)} - \text{CFD}_{i}^{(j)}\right)^{2}}}{\text{Max}\left(\text{CFD}^{(j)}\right) - \text{Min}\left(\text{CFD}^{(j)}\right)} \times 100 \qquad (21)$$

where i corresponds to the ith nodal value of heat flux on the panel, j corresponds to the jth evaluation case, and p is the total number of nodes on the panel. In addition, the L_{∞} error is also considered:

$$L_{\infty}^{(j)}(\%) = \frac{\text{Max}\left(\left|\text{Surrogate}^{(j)} - \text{CFD}^{(j)}\right|\right)}{\text{Max}\left(\text{CFD}^{(j)}\right) - \text{Min}\left(\text{CFD}^{(j)}\right)} \times 100 \qquad (22)$$

where j again corresponds to the jth evaluation case. Note that these errors are normalized by the difference between the maximum and minimum values of a single evaluation case. These error metrics are computed for each evaluation case, resulting in a vector of 500 NRMSE and L_{∞} values for each surrogate developed.

In order to provide a scalar quantification of the model quality, the average NRMSE, average L_{∞}, overall max L_{∞}, and the percent of evaluation cases with less than 10% L_{∞} error for the three sets of 500 evaluation cases are computed for each surrogate. The results from this assessment are shown in Fig. 5. As expected, the accuracy of the surrogate increases with increasing the number of sample points. However, the rate of improvement decreases significantly after 800 sample points. For 1200 sample points the average NRMSE is 2% and 90% percent of evaluation cases have less than 10% L_{∞} error. Note that there are relatively small differences in accuracy of the surrogate when the surface temperature profile of the actual solution differs from the third-order polynomial used to construct the surrogate. This suggests that the assumed third-order spatial variation in surface temperature captures the prominent impact of spatial variations in surface temperature on the aerodynamic heating. Furthermore, this also suggests that a lower order polynomial may be appropriate for parameterizing spatial surface temperature variations, enabling a reduction in the parameter space. Finally, it is clear that the error introduced by using a surrogate in place of CFD is small compared to general uncertainty associated with aerodynamic heating and turbulence modeling in hypersonic flow.

3.2   Aerodynamic Pressure

3.2.1   Assessment of Surrogate Accuracy for Steady-State Aerodynamic Pressure

The accuracy of the developed surrogate framework for modeling CFD predictions of the steady-state pressure is assessed in a similar manner to aerodynamic heating. Thus, surrogates constructed using 100, 400, 800, and 1200 sample points are compared against the three sets of 500 evaluation cases that randomly cover the input parameter space in Tables 2 and 4. As before, the accuracy of the surrogate is quantified using the average NRMSE, average L_{∞}, overall max L_{∞}, and percent of evaluation cases with less than 10% L_{∞} relative to each of the 500 evaluation cases. The results from this assessment are shown in Fig. 6. For 1200 sample points the average NRMSE is 2%, and 95% of the evaluation cases have less than 10% L_{∞} error. Note that the errors are all similar in trend and magnitude to those for the aerodynamic heating predictions of the surrogate, shown in Fig. 5.

3.2.2   Comparison of Modeling Approaches for the Steady-State Pressure

Similar to aerodynamic heating, different modeling approaches are compared for steady-state pressure prediction, such as: 1) third-order piston theory, 2)
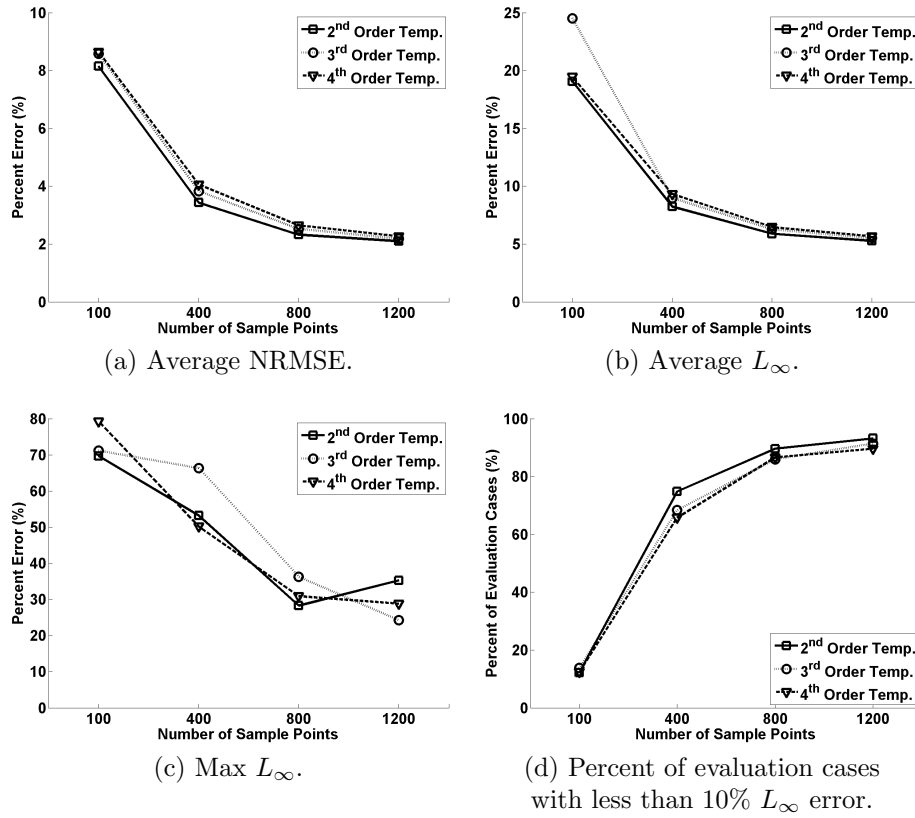
(a) Average NRMSE.

(b) Average L_∞.

(c) Max L_∞.

(d) Percent of evaluation cases with less than 10% L_∞ error.

Figure 5: Assessment of surrogate accuracy for aerodynamic heating relative to three different sets of 500 CFD evaluation cases.

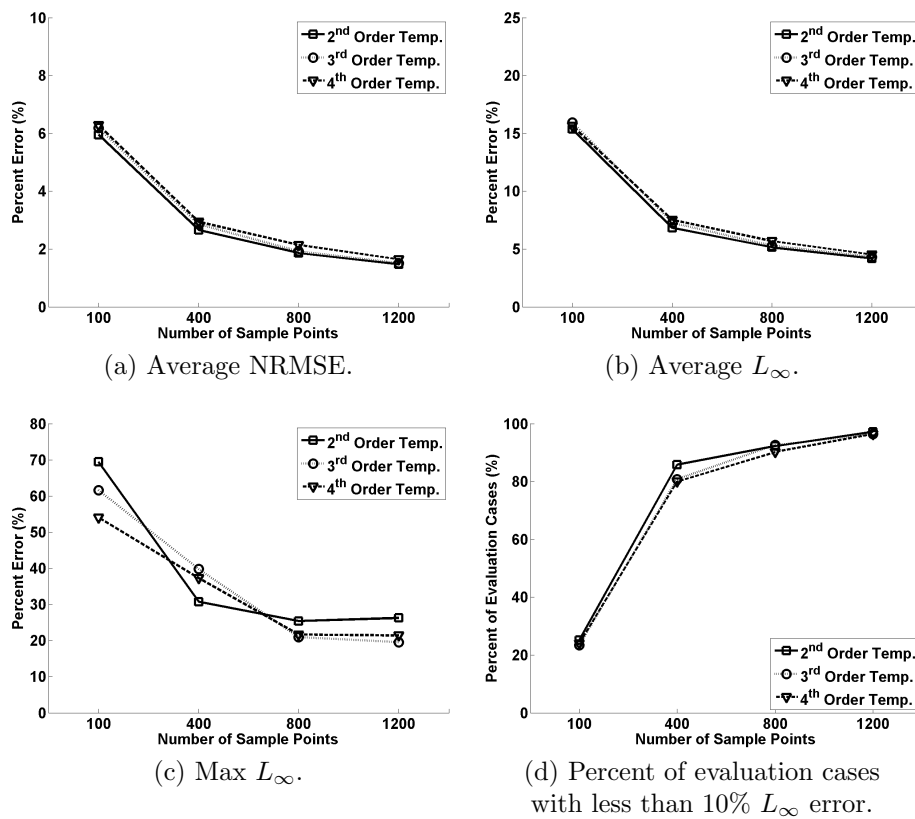(a) Average NRMSE.
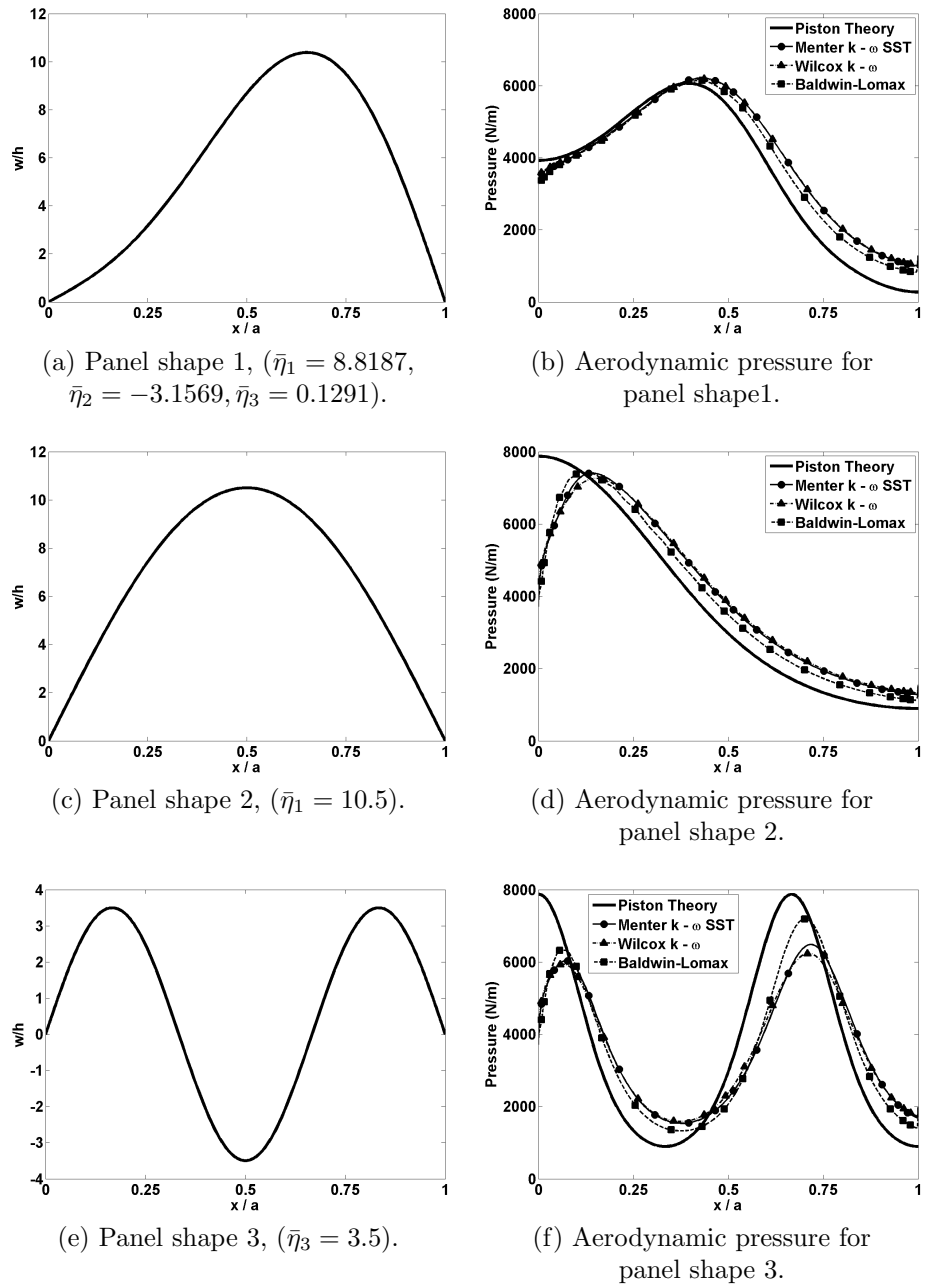
(b) Average L_∞.

(c) Max L_∞.

(d) Percent of evaluation cases with less than 10% L_∞ error.

Figure 6: Assessment of surrogate accuracy for aerodynamic pressure relative to three different sets of 500 CFD evaluation cases.

(a) Panel shape 1, ($\bar{\eta}_1 = 8.8187$, $\bar{\eta}_2 = -3.1569, \bar{\eta}_3 = 0.1291$).

(b) Aerodynamic pressure for panel shape1.

(c) Panel shape 2, ($\bar{\eta}_1 = 10.5$).

(d) Aerodynamic pressure for panel shape 2.

Figure 7: Comparison of aerodynamic pressure predictions for several panel shapes, $M_1 = 8.0$ at 30 km.

(e) Panel shape 3, ($\bar{\eta}_3 = 3.5$).

(f) Aerodynamic pressure for panel shape 3.

RANS with Menter $k - \omega$ SST turbulence model, 3) RANS with Wilcox $k - \omega$ turbulence model, and 4) RANS with Baldwin–Lomax turbulence model. The same temperature profile shown in Fig. 3 is applied to the same three panel deformations from the aerodynamic heating comparisons. As before, the details for computing the aerodynamic pressure using piston theory are provided in [7].

The aerodynamic pressure solutions for these deformations are shown in Figs. 7(b,d,f), respectively. Maximum and average differences between the different models and the RANS with Menter $k - \omega$ SST turbulence model are provided in Table 5. Several general conclusions can be made from these results. First, it is clear from Fig. 7(d,f) that the largest errors occur at the leading edge of the panel. These errors correlate with the degree of surface inclination at the leading edge between the three different panel shapes. In addition, for all three shapes, piston theory under predicts the pressure relative to the CFD solutions in panel regions with negative slope. Also note that there is a shift in the peak pressure location between the CFD and piston theory solutions. Each of these

	Piston Theory Menter	Wilcox Menter	Baldwin-Lomax Menter	Surrogate Menter
Max.	76.6%	5.99	18.78	1.53
Avg.	25.7%	1.64	7.65	0.57

Table 5: Comparison of steady aerodynamic pressure predictions using different modeling approaches.

discrepancies between piston theory and the CFD approaches can likely be attributed to the boundary layer displacement effect not accounted for in piston theory, which is inviscid. In contrast to the aerodynamic heating, variation in the aerodynamic pressure predictions for each turbulence model were relatively minor ($< 8\%$ average difference). Furthermore, as with aerodynamic heating, the surrogate error was small ($< 2\%$) relative to the variation introduced by using different turbulence models.

3.2.3 Comparison of Modeling Approaches for Predicting the Unsteady Aerodynamic Pressure

A comparison of the GAFs is provided in Fig. 8 for the 1200 sample point surrogate, third-order piston theory, unsteady Euler, and unsteady Navier-Stokes aerodynamics. Equation 23 is used to compute the GAFs,

$$GAF(t) = \int \left(\Phi(x) q_a(x,t) \right) dx \qquad (23)$$

where $\Phi(x)$ is the mode shape, and Eq. 10 is used for the surrogate unsteady pressure prediction. Three different panel shapes are considered, each vibrating at a frequency of 140 Hz. This frequency was selected based on the post flutter response computed in [7] for a panel operating at an altitude of 30 km and Mach 10.0. The first panel shape in Fig. 8(a) is the first panel mode, the second shape in Fig. 8(c) is the second mode, and the third shape in Fig. 8(e) is a linear superposition of the first three panel modes. Note that the surface temperature is set to a uniform 1200 K.

Several interesting items can be noted from this comparison. First, it is clear that GAFs computed using piston theory and Euler aerodynamics are in good to excellent agreement for the three cases considered. However, neither follow the Navier-Stokes prediction. This indicates that boundary layer displacement effects significantly impact the generalized aerodynamic forces of panels. Note this is consistent with findings by Nydick et al[35] for oscillating panels in hypersonic flow. In contrast to the inviscid modeling, the surrogate closely follows the Navier-Stokes prediction. Specifically, the NRMSE error of the surrogate relative to the Navier-Stokes prediction is between 3 - 5%, while the L_∞ error is between 6 - 8%. It is important to note that, in results not shown, the prediction of the surrogate without correction using the unsteady pressure terms in Eqs. 8 and 9 had NRSME errors between 4 - 14%, and L_∞ errors between 8 - 21%. Similar to Ref. [30], these results indicate that the primary flow nonlinearities in hypersonic flow are captured using steady-state analysis, and that unsteady effects can be approximated using basic theoretical unsteady aerodynamics such as piston theory.

4. Aerothermoelastic Method of Solution

As indicated previously, the thermo-elastic panel model used in this study was developed previously by Culler and McNamara[7]. This paper also follows the partitioned aerothermoelastic solution process descibed in [7]. For brevity, these are only summarized here. For a complete description, including verification and validation of the model and approach, refer to [7].
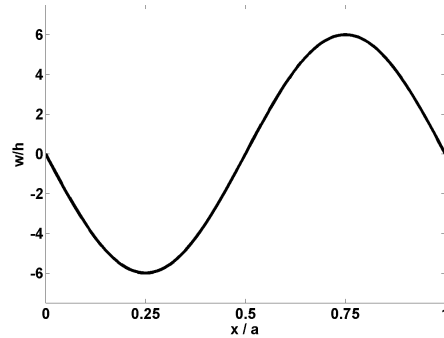
The framework of the aerothermoelastic model, shown in Fig. 9, is divided into aerothermal and aeroelastic components. The structural temperature dis-
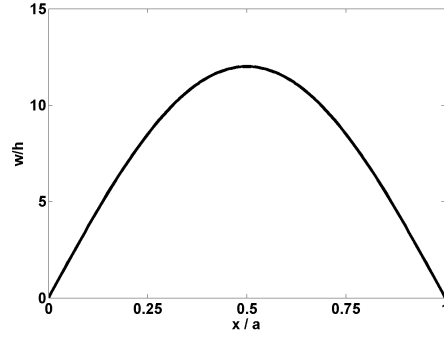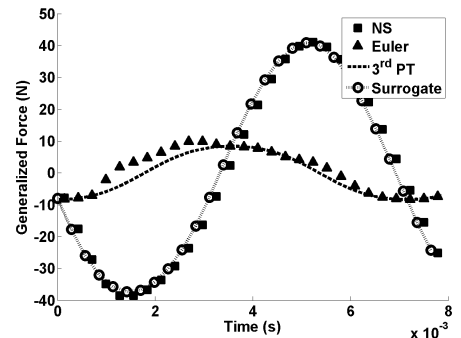
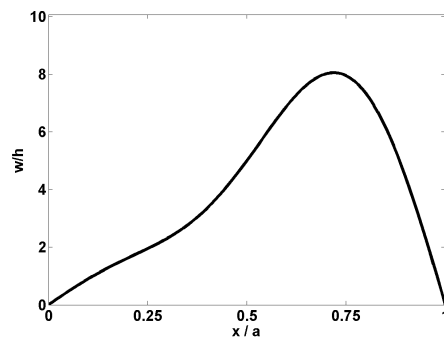(a) First panel mode, ($\bar{\eta}_1$=12).
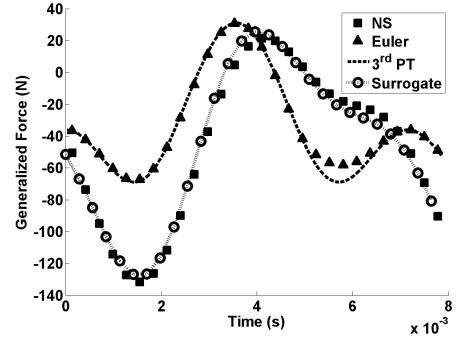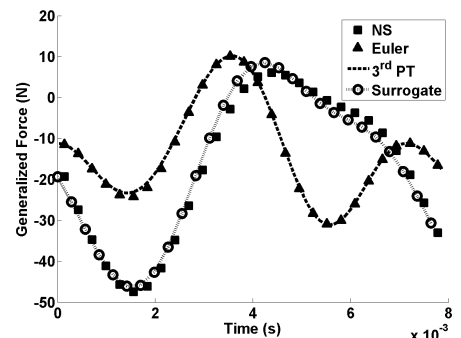

(b) Generalized force, for the first mode.

(c) Second panel mode, ($\bar{\eta}_2$=6).

(d) Generalized force, for the second mode.

Figure 8: Generalized force comparisons for the panel oscillating at 140 Hz, $M_1 = 10$, 30 km, and a uniform temperature of 1200 K.

(e) Linear superposition of the first three panel modes, ($\bar{\eta}_1$=6, $\bar{\eta}_2$=-3, $\bar{\eta}_3$=1).

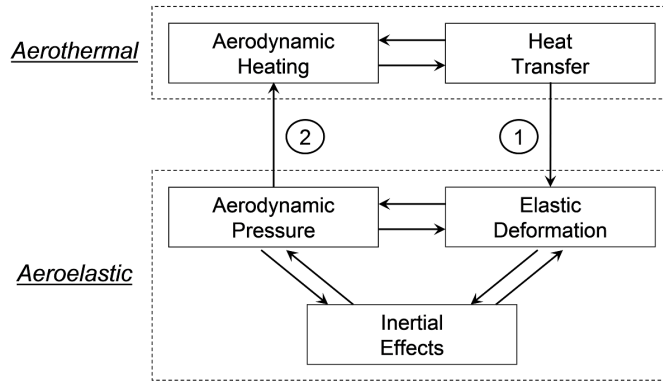(f) Generalized force, for linear superposition of the first three modes.

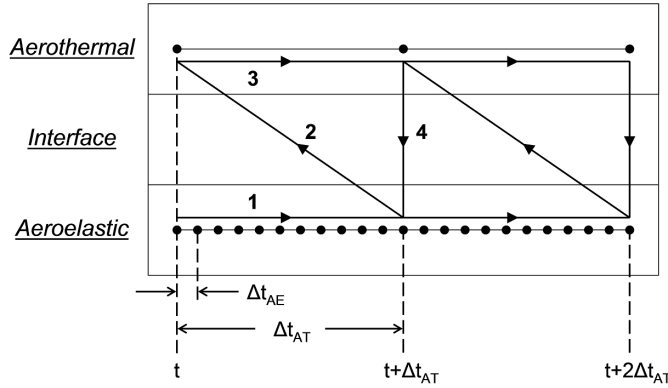**Figure 9:** Components of the aerothermoelastic model [7].

Figure 10: Aerothermoelastic solution using a partitioned approach to couple aerothermal and time-averaged aeroelastic solutions [7].

tribution is passed from the aerothermal solution to the aeroelastic problem in path (1). Feedback of elastic deformation to the aerothermal problem is transferred in path (2). The partitioned time-marching approach is illustrated in Fig. 10. Step (1) is a time marching solution of the aeroelastic problem to proceed from time t to time $t + \Delta t_{AT}$. In step (2) the elastic deformation that occurred during step (1) is passed to the aerothermal model in a time-averaged sense[7]. Step (3) is a time marching solution of the aerothermal problem to proceed from time t to time $t + \Delta t_{AT}$. Finally, in step (4) the structural temperature distribution is updated in the aeroelastic model. Note that different steps sizes are used for the aerothermal and aeroelastic time marching process.

The structural equation of motion is based on a 2-D von Kármán panel [7]:

$$\frac{\partial^2}{\partial x^2}\left(D\frac{\partial^2 w}{\partial x^2}\right) - N_x\frac{\partial^2 w}{\partial x^2} + \left(\sum_i h_i\rho_i\right)\frac{\partial^2 w}{\partial t^2} + q_a + \frac{\partial^2 M_T}{\partial x^2} = 0 \qquad (24)$$

This equation of motion is discretized using Galerkin's method to replace the spatial dependence with a summation of six assumed sine modes. The resulting system of nonlinear, ordinary differential equations is integrated directly in the time domain using a fourth order Runge-Kutta method [7].

Transient heat transfer to the panel is computed using the a finite difference solution to the 2-D heat equation for the chord-wise and through-thickness directions [7]:

$$\rho c\frac{\partial T}{\partial t} = k_x\frac{\partial^2 T}{\partial x^2} + k_z\frac{\partial^2 T}{\partial z^2} \qquad (25)$$

As shown in Fig. 11, the thermal model for the thermal protection system and panel is assumed to consist of three layers: 1) a radiation shield (PM-2000 honeycomb sandwich), 2) thermal insulation (internal multi-screen insulation), and 3) panel structure (a high temperature grade titanium alloy). Boundary
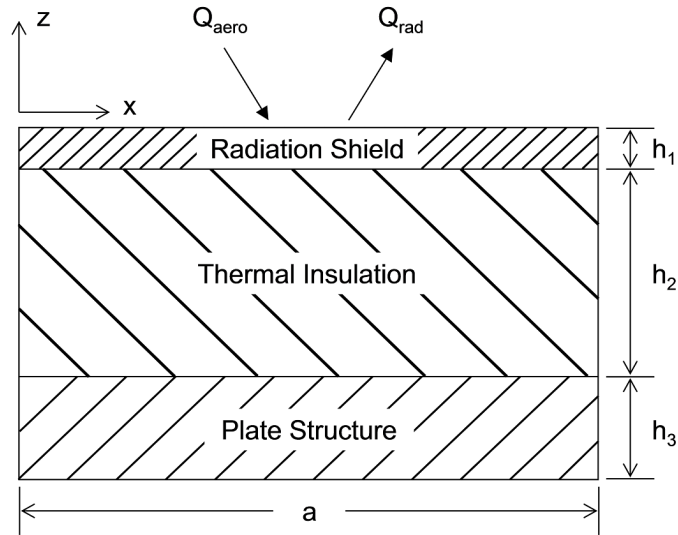
Figure 11: Two-dimensional model of the thermal structure [7].

Table 6: Properties of the thermal structure at 300 K [7].

	ρ (kg/m^3)	c $(J/kg/K)$	k $(W/m/K)$	h_i (mm)
Radiation Shield	1010	465	0.250	2.0
Thermal Insulation	73.0	729	0.0258	10.0
Plate Structure	4540	463	6.89	5.0

conditions for the thermal model consist of aerodynamic heating and thermal radiation at the upper surface of the radiation shield, and adiabatic conditions at the panel edges and bottom surface. The thermophysical properties and thickness of each layer are listed in Table 6. Note that specific heat and thermal conductivity are temperature dependent. Data for these properties as a function of temperature are provided by Ref. [34] for the radiation shield and the thermal insulation, and by Ref. [33] for the plate structure. Finally, note that the mass of the thermal protection system is included in Eq. 24, but the stiffness is neglected.

The computation of the generalized aerodynamic forces, from Eq. 23, on the panel requires spatial integration of the surface pressure, where C_p is computed using Eq. 7. This integration is carried out numerically with a two point Gaussian quadrature with 500 surface elements since this yielded convergence of the aerothermoelastic flutter boundary within 0.12% at Mach 10.5 when compared to a 1000 surface element integration. Consistent with Culler and McNamara[7], only deformation induced pressures are included in the aerothermoelastic analysis. Thus, the non-zero, stream-wise pressure variations on the underformed panel surface, that occur due to boundary layer displacement effects, are removed by subtracting the undeformed surface pressure at each time step of the aerothermoelastic analysis.

5. Aerothermoelastic Analysis

In this section the aerothermoelastic response of the panel is computed using Eqs. 6 and 7 with a CFD surrogate constructed from 1200 sample points. These results are compared with those computed by Culler and McNamara[7] (C-M), who used third-order piston theory and Eckert's reference enthalpy to model the aerothermodynamics, in order to assess the impact of modeling fidelity on panel response during a coupled analysis. Comparisons between the different modeling approaches are made for the flutter boundary, dynamically stable aerothermoelastic response, and post-flutter aerothermoelastic response, respectively. The panel configuration and operating conditions used for aerothermoelastic analysis

Altitude	30 km
Freestream Mach Number	7.5 – 10.5
Initial Panel Temperature	300 K

Mach Number	C-M (seconds)	Surrogate (seconds)	Difference (%)
$M_1 = 7.5$	1672.0	1658.8	-0.8
$M_1 = 8.0$	956.2	1016.4	6.3
$M_1 = 8.5$	515.0	591.8	14.9
$M_1 = 9.0$	274.8	354.3	28.9
$M_1 = 9.5$	140.6	219.0	55.8
$M_1 = 10.0$	73.0	140.5	92.4
$M_1 = 10.5$	40.7	100.3	146.7

Table 7: Parameters used to compute the aerothermoelastic response of a skin panel.

Table 8: Comparison of flight times to the onset of flutter predicted using surrogate and analytical modeling approaches.

are listed in Table 7.

5.1 Aerothermoelastic Flutter Boundary

The flight time to the onset of flutter for the panel for seven different constant Mach number trajectories is shown in Table 8. As discussed in Ref. [7], the higher the freestream Mach number, the shorter the onset time to panel flutter. It is interesting that the differences between the analytical and surrogate aerothermodynamic modeling approaches decrease with freestream Mach number. At the highest Mach number considered ($M_1 = 10.5$), the difference between the two methods is over 100%; while at the lowest Mach number considered ($M_1 = 7.5$), the difference is less than 1%. Furthermore, for $8.0 \leq M_1 \leq 10.5$, the analytical modeling approach yields a conservative estimate for the flutter boundary. However, at $M_1 = 7.5$, the surrogate produces a slightly conservative estimate. Further insight into the sources of differences between the flutter boundaries is provided by a comparison of the dynamically stable aerothermoelastic panel response discussed next.

5.2 Dynamically Stable Aerothermoelastic Response

Snap shots of the dynamically stable aerothermoelastic panel response are shown in Fig. 12 and 13, and differences between the surrogate-based model and the C-M results near flutter are quantified in Tables 9 and 10 for the $M_1 = 7.5$ and 10.5 trajectories, respectively. These two trajectories are chosen since they resulted in the least and greatest difference between the analytical and surrogate aerothermodynamic models in terms of flight time to the onset of flutter. Four different quantities are considered for each trajectory: pressure differential, aerodynamic heat flux, panel displacement, and mid-plate temperature. The first two quantities represent the driving loads in the system, while the second two represent the panel response. For the $M_1 = 7.5$ trajectory, there are modest differences in the panel loads and response between the surrogate and C-M cases. For example, the average differences between the two models are all under 13% and maximum differences are under 20%. For the $M_1 = 10.5$ case, there are larger differences between the surrogate-based model and C-M results in terms of panel displacement and heat flux, similar differences in pressure, and smaller differences in the mid-plate temperature. The difference in the aerodynamic heat flux is relativley high, averaging 20.7%, however the difference in the mid-plate temperature is very small, due to the short time duration. Also note, differences in panel displacement near flutter are much higher for $M_1 = 10.5$, max of 32.7%, versus the $M_1 = 7.5$ case, max of 4.2%.

While these comparisons demonstrate some increased differences between the surrogate and analytical models at the different Mach numbers, they do not
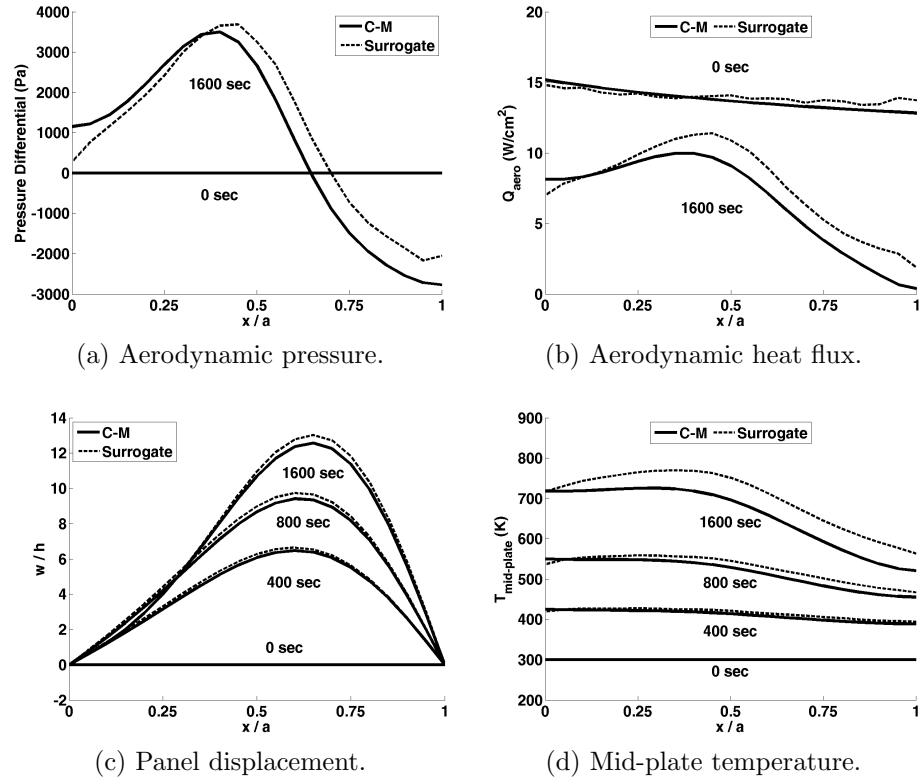
(a) Aerodynamic pressure.

(b) Aerodynamic heat flux.

(c) Panel displacement.

(d) Mid-plate temperature.

Figure 12: Pressure, heating, panel displacement, and thermal loads during dynamically stable aerothermoelastic response at $M_1 = 7.5$.

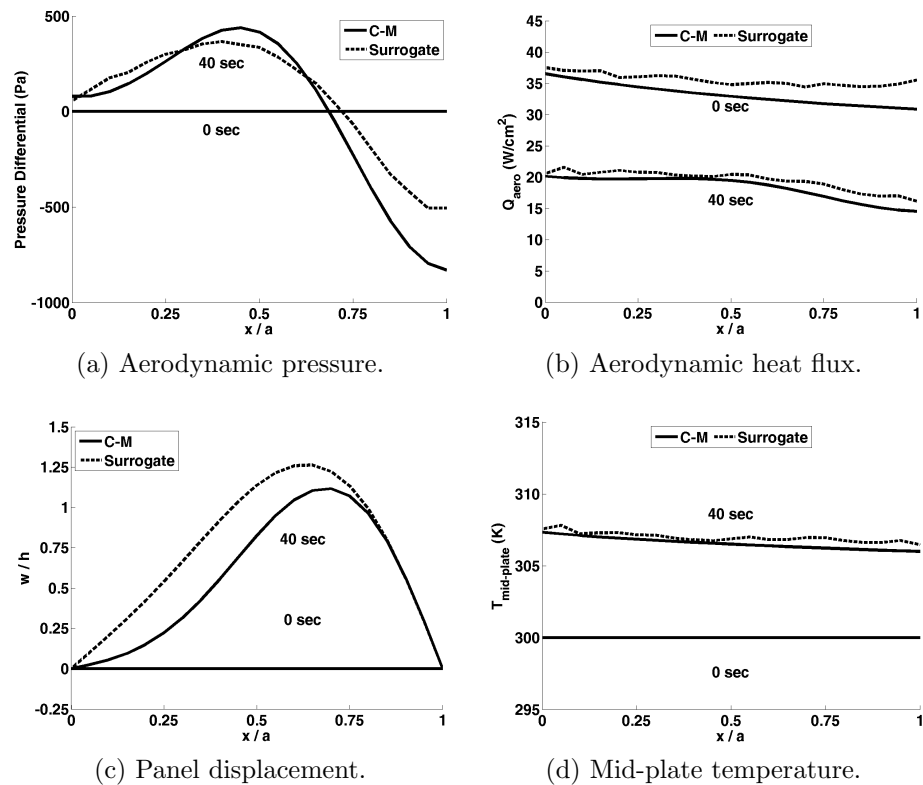(a) Aerodynamic pressure.

(b) Aerodynamic heat flux.

(c) Panel displacement.

(d) Mid-plate temperature.

Figure 13: Pressure, heating, panel displacement, and thermal loads during dynamically stable aerothermoelastic response at $M_1 = 10.5$.

	Average (%) Difference	Max (%) Difference	Location of Max (% of Panel Length)
Pressure	8.3	15.1	62.0
Heat Flux	12.6	19.9	57.1
Displacement	2.6	4.2	71.4
Mid-plate Temp.	4.6	8.9	95.2

Table 9: Percent difference between the surrogate-based and C-M models for pressure, heating, panel displacement, and thermal loads for $M_1 = 7.5$ at 1600 sec.

	Average (%) Difference	Max (%) Difference	Location of Max (% of Panel Length)
Pressure	7.5	22.6	90.5
Heat Flux	20.7	35.4	76.2
Displacement	20.3	32.7	19.0
Mid-plate Temp.	0.13	0.24	95.2

Table 10: Percent difference between the surrogate-based and C-M models for pressure, heating, panel displacement, and thermal loads for $M_1 = 10.5$ at 40 sec.

fully explain the large discrepancy in onset time to flutter at $M_1 = 10.5$ between the surrogate-based and theoretical cases. However, a comparison of the relative magnitude of each quantity at Mach 10.5 and 7.5, shown in Fig. 14, provides additional insight. Note that the $M_1 = 7.5$ trajectory results in significantly higher panel displacements, mid-plate temperatures, and pressure differentials, but smaller surface heat flux. The lower heat flux is due to operation at a lower freestream Mach number at Mach 7.5 compared to $M_1 = 10.5$. Despite the lower heating rate, the significantly delayed flutter of the panel at $M_1 = 7.5$ compared to $M_1 = 10.5$ results in the panel ultimately reaching a higher temperature. The fact that the $M_1 = 7.5$ case withstands higher pressure prior to loss of dynamic stability compared to the $M_1 = 10.5$ case, while at a significantly elevated temperature, is counter-intuitive. This indicates that the $M_1 = 7.5$ panel case experiences significant stiffening during post-buckling as a result of the in-plane thermal force, and that the rate of stiffening occurs at a faster rate than the accumulation of pressure loading and reduction in Young's modulus due to temperature. This ultimately enables the panel to sustain higher pressure loading prior to initiating limit cycle oscillations. Such an explanation is supported by previous research[24, 36], which has shown that fundamental frequencies of simply-supported beams and plates increase with increasing in-plane thermal load during post-buckled displacements. Since the panel is stiffer at $M_1 = 7.5$, compared to $M_1 = 10.5$, it is less sensitive to differences in pressure between the surrogate-based model and C-M model, reducing the difference in the onset time to flutter.

5.3 Nonlinear Aerothermoelastic Post-Flutter Response

A comparison of the nonlinear aerothermoelastic panel flutter response, represented using the panel displacements at the 75% chord, is shown in Figs. 15 and 16 for the $M_1 = 7.5$ and $M_1 = 10.5$ trajectories, respectively. The displacement envelopes, representing the maximum and minimum panel displacement at the 75% chord, are shown in Figs. 15(a) and 16(a). Following [7], four distinct regions of response are evident, namely: 1) initially flat and stable, followed by 2) dynamically stable deformation, before 3) the onset of flutter, and a transition to 4) limit cycle oscillations. In Fig. 16(a), the panel response computed using the surrogate-based aerothermoelastic model remains in the buckled but dynamically stable configuration much longer than predicted in [7]. Thus, at the point that oscillations begin, the surrogate-based model starts from a larger deformation, which impacts the post flutter response and limit cycle oscillations.

The post flutter oscillations for each Mach number are shown in Figs. 15(b)
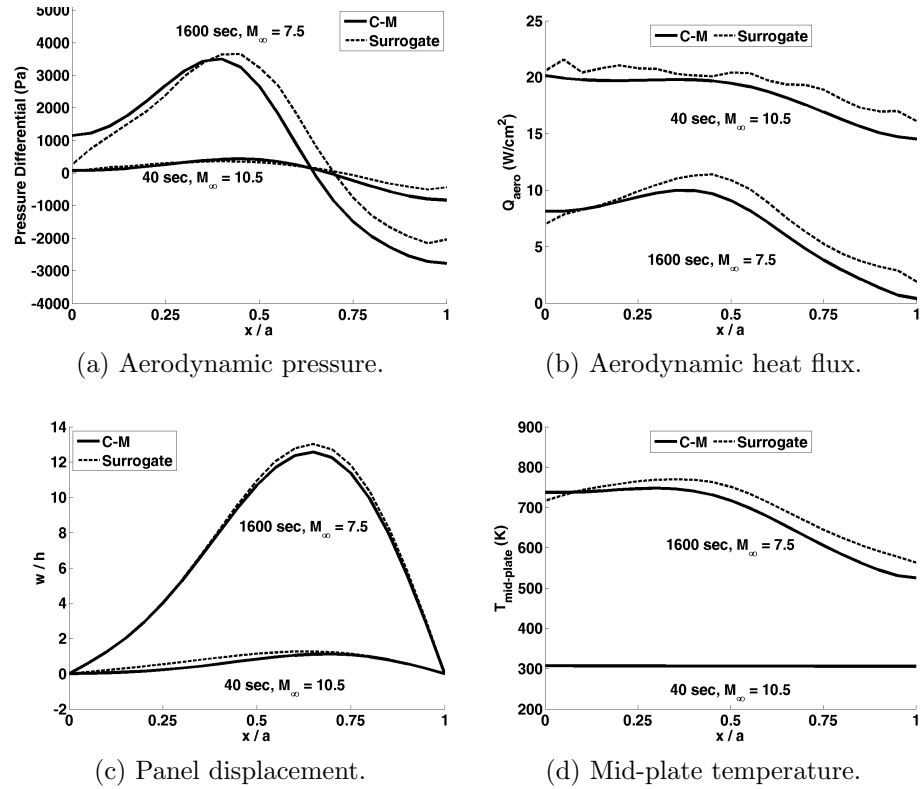
(a) Aerodynamic pressure.

(b) Aerodynamic heat flux.

Figure 14: Pressure, heating, panel deformation, and thermal loads near the onset time of flutter for both the $M_1 = 7.5$ and $M_1 = 10.5$ trajectories.
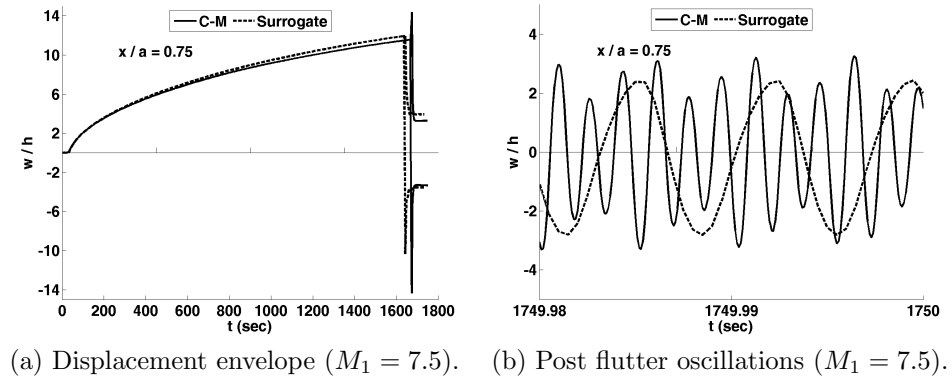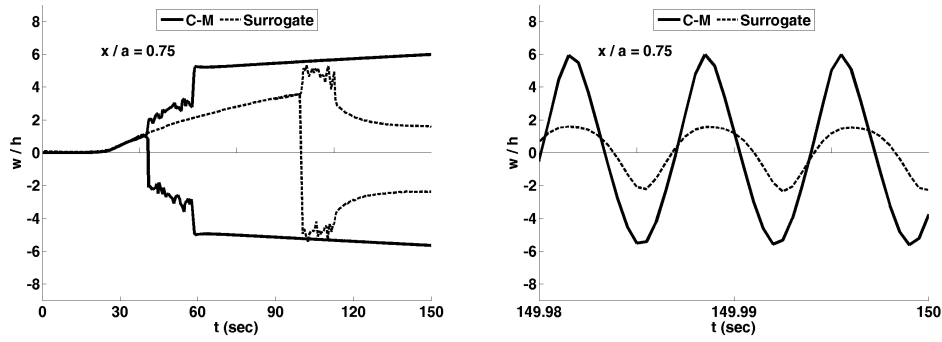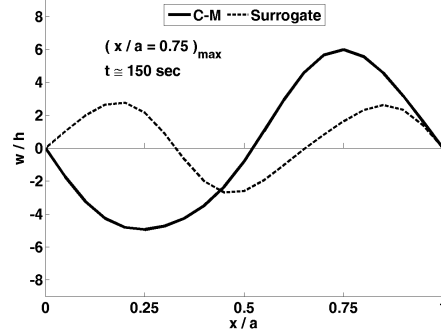

(c) Panel displacement.

(d) Mid-plate temperature.

(a) Displacement envelope ($M_1 = 7.5$).

(b) Post flutter oscillations ($M_1 = 7.5$).

Figure 15: Nonlinear aerothermoelastic panel flutter response at $M_1 = 7.5$.

(c) Instantaneous deformation ($M_1 = 7.5$).

(a) Displacement envelope ($M_1 = 10.5$).   (b) Limit cycle oscillations ($M_1 = 10.5$).

(c) Instantaneous deformation ($M_1 = 10.5$).

Figure 16: Nonlinear aerothermoelastic panel flutter response at $M_1 = 10.5$.

and 16(b), and the instantaneous panel deformation during limit cycle oscillation is illustrated in Figs. 15(c) and 16(c). Note that the time scale in Figs. 15(b) and 16(b) are reduced compared to Figs. 15(a) and 16(a) in order to clearly discern the oscillations. In Figs. 15(c) and 16(c) the surrogate-based model oscillations are dominated by the third panel mode, whereas for C-M in Fig. 15(c) the oscillations are dominated by the fifth mode, and in Fig. 16(c) the oscillations are dominated by the second mode. For the $M_1 = 10.5$ response, comparing the limit cycle oscillations, Fig. 16(b), to the instantaneous deformation during limit cycle oscillations, Fig. 16(c), reveals that both models predict roughly the same frequency of oscillation, 140 Hz for C-M vs. 135 Hz for the surrogate-based model, even though they have different dominant modes, and different amplitudes of oscillation. For the $M_1 = 7.5$ response, Figs. 15(b,c), the surrogate-based model again predicts the frequency of oscillation to be approximately 135 Hz, while C-M predicted approximately 625 Hz. Note that the frequency and slope of the $M_1 = 7.5$ post-flutter response exceed the well-known limits of piston theory[7, 30]; thus the discrepancy in these results is not surprising.

5.4 Computational Requirements for Aerothermoelastic Analysis

In order to further compare the different modeling approaches, this section discusses computational requirements for different aerothermodynamic modeling approaches in the context of aerothermoelastic analysis. The computational expense of analytical, CFD surrogate, and standard CFD are compared in Table 11. Note that these computational times are based on a time-step size of 0.0005 sec for the aeroelastic analysis, and 0.1 sec for the aerothermal analysis[7]. The first column represents the computational time required to generate one solution of the pressure and the heat flux. For the CFD analysis this number is approximated from the time required for one time step in an unsteady analysis, starting from a converged steady-state solution. One aeroelastic (AE) - aerothermal (AT) cycle represents the time required to proceed through the en-

Table 11:
Computational cost of different aerothermodynamic modeling approaches.

Model	1 Iteration of Aero Loads (seconds)	1 AE - AT Cycle[c] (min)	1500 seconds of Response (hours)
C-M	0.0845[b]	0.081[b]	20.30[b]
Surrogate	0.0227[b]	0.217[b]	54.30[b]
Full-Order CFD	4.20[a]	56.1[a,d]	14,000[a,d]

[a] Eight 2.60 GHz Opteron processors, 2.0 GB RAM each.
[b] One 2.60 GHz Opteron processor, 2.0 GB RAM.
[c] 1/10th of a second of response: 1 AT time step, 200 AE time steps.
[d] Projected time.

tire model once (1/10th of a second of response). The final column represents the computational time required to produce 1500 seconds of aerothermoelastic response.

Note that one AE-AT cycle for the surrogate method takes approximately two and a half times longer than the theoretical modeling used in [7] due to differences in spatial integration of the surface pressure during the Runge-Kutta time marching of Eq. 24. Recall that the surrogate approach requires a numerical integration of the pressure, while in [7] the GAFs were computed using an exact integration of the piston theory pressure prior to time-marching. While the surrogate is more expensive relative to the theoretical aerothermodynamic approach, it is still several orders of magnitude more efficient than a standard CFD solution. For the present analysis, the use of CFD within aerothermoelastic analysis is impractical for the response times shown in Table 8 (e.g., up to approximately 30 minutes of response). Finally, note that the computational overhead required to generate the 1200 sample points for the surrogate is relatively small at 12 hours on 80 2.60 GHz Opteron processors.

6.   Conclusions

The studies on modeling of hypersonic aerothermodynamics using CFD surrogates allows one to reach several useful conclusions:

1. Kriging in conjunction with a Latin Hypercube sampling provides an accurate and robust method for constructing aerothermodynamic surrogates for hypersonic flow.

2. There can be up to a 60% variation in aerodynamic heating predictions and 20% variation in aerodynamic pressure predictions associated with turbulence modeling in hypersonic flow.

3. Boundary layer displacement effects significantly impact chordwise aerodynamic heating profiles and the unsteady aerodynamic pressures on skin panels in hypersonic flow.

4. Unsteady generalized aerodynamic forces on vibrating 2-D panels can be accurately modeled using steady-state CFD augmented with unsteady terms from simple analytical theories such as piston theory.

5. The use of CFD surrogates, in place of theoretical aerothermodynamic model approaches for hypersonic aerothermoelastic analysis of panels, can result in over 100% difference in the onset time to flutter. Furthermore, the predicted post-flutter response is highly sensitive to the aerothermodynamic model approach used.

6. The developed surrogate approach provides a reasonably accurate and computationally efficient approach for incorporating computational fluid dynamics solutions for the aerothermodynamic loads into a dynamic, long time-record aerothermoelastic analysis. Due to the high computational cost of CFD, reduced-order modeling is the only practical means for CFD based aerothermoelastic analysis over long time record hypersonic trajectories.

7. Acknowledgments

References

[1] J. D. Anderson, Jr. *Modern Compressible Flow with Historical Perspective.* McGraw-Hill, New York, third edition, 2003.

[2] J. D. Anderson, Jr. *Hypersonic and High-Temperature Gas Dynamics.* American Institute of Aeronautics and Astronautics, Reston, Virginia, second edition, 2006.

[3] H. Ashley and G. Zartarian. Piston Theory - A New Aerodynamic Tool for the Aeroelastician. *Journal of the Aeronautical Sciences*, 23(12):1109–1118, December 1956.

[4] R. E. Bartels, C. L. Rumsey, and R. T. Biedron. CFL3D User's Manual - General Usage and Aeroelastic Analysis (Version 6.4). NASA TM 2006-214301, 2006.

[5] J. J. Bertin and R. M. Cummings. Critical Hypersonic Aerothermodynamic Phenomena. *Annual Review of Fluid Mechanics*, 38:129–157, January 2006.

[6] G. V. Candler, D. J. Mavriplis, and L. Trevino. Current Status and future Prospects for the Numerical Simulation of Hypersonic Flows. AIAA Paper 2009-153, January 2009. 47th AIAA Aerospace Sciences Meeting.

[7] A. J. Culler and J. J. McNamara. Studies on Fluid-Thermal-Structural Coupling for Aerothermoelasticity in Hypersonic Flow. *AIAA Journal*, 48(8):1721–1738, August 2010.

[8] A. J. Culler and J. J. McNamara. Coupled Flow-Thermal-Structural Analysis for Response Prediction of Hypersonic Vehicle Skin Panels. *AIAA Journal*, Submitted May 2010. In Review - see AIAA-2010-2965.

[9] J. R. DeBonis, L. Oberkampf, W., R.T. Wolf, P.D. Orkwis, M.G. Turner, and H. Babinsky. Assessment of CFD Models for Shock Boundary-Layer Interaction. 28th AIAA Applied Aerodynamics Conference, AIAA Paper 2010-4823, July 2010.

[10] F. R. DeJarnette, H. H. Hamilton, K. J. Weilmuenster, and F. M. Cheatwood. A Review of Some Approximate Methods Used in Aerodynamic Heating Analyses. *Journal of Thermophysics and Heat Transfer*, 1(1):5–12, January 1987.

[11] E. H. Dowell and K. C. Hall. Modeling of Fluid-Structure Interaction. *Annual Review of Fluid Mechanics*, 33:445–490, 2001.

[12] J. Dugundji and J. M. Calligeros. Similarity Laws for Aerothermoelastic Testing. *Journal of the AeroSpace Sciences*, 29(8):935–950, August 1962.

[13] E. R. G. Eckert. Engineering Relations for Heat Transfer and Friction in High-Velocity Laminar and Turbulent Boundary-Layer Flow Over Surfaces With Constant Pressure and Temperature. *Transactions of the ASME*, 78(6):1273–1283, August 1956.

[14] N. Falkiewicz, C. E. S. Cesnik, A. R. Crowell, and J. J. McNamara. Reduced-Order Aerothermoelastic Framework for Hypersonic Vehicle Control Simulation. *AIAA Journal*, Accepted April 2011. In Review, preprint available upon request.

[15] B. Glaz, L. Liu, and P. P. Friedmann. Reduced-Order Nonlinear Unsteady Aerodynamic Modeling Using a Surrogate Based Recurrence Framework. *AIAA Journal*, 48(10):2418–2429, 2010.

[16] B. Glaz, L. Liu, P. P. Friedmann, J. Bain, and L. Sankar. A Surrogate Based Approach to Reduced-Order Dynamic Stall Modeling. AIAA Paper 2010-3042, April 2010.

[17] K. C. Hall, J. P. Thomas, and E. H. Dowell. Proper Orthogonal Decomposition Technique for Transonic Unsteady Aerodynamic Flows. *AIAA Journal*, 38(10):1853–1862, October 2000.

[18] H. H. Hamilton, F. A. Greene, and F. R. DeJarnette. Approximate Method for Calculating Heating Rates on Three-Dimensional Vehicles. *Journal of Spacecraft and Rockets*, 31(3):345–354, May–June 1994.

[19] P. Hartwich and S. Agrawal. Perturbing Multiblock Patched Grids in Aeroelastic Design Optimization Applications. AIAA Paper 1997-2038, June 1997.

[20] J. Hilsenrath, H. J. Hoge, C. W. Beckett, J. F. Masi, W. S. Benedict, R. L. Nuttall, L. Fano, Y. S. Touloukian, and H. W. Woolley. *Tables of Thermodynamic and Transport Properties of Air, Argon, Carbon Dioxide, Carbon Monoxide, Hydrogen, Nitrogen, Oxygen, and Steam.* Pergamon Press, New York, 1960.

[21] D. J. Kinney, J. A. Garcia, and L. Huynh. Predicted Convective and Radiative Aerothermodynamic Environments for Various Reentry Vehicles Using CBAERO. AIAA Paper 2006-659, January 2006.

[22] S. L. Krist, R. T. Biedron, and C. L. Rumsey. CFL3D User's Manual (Version 5.0). NASA TM 1998-208444, 1997. CFL3D Version 6.0 update: `http://cfl3d.larc.nasa.gov/Cfl3dv6/cfl3dv6.html`.

[23] N. Lamorte, B. Glaz, P. P. Friedmann, A. J. Culler, A. R. Crowell, and J. J. McNamara. Uncertainty Propagation in Hypersonic Aerothermoelastic Analysis. AIAA Paper 2010-2964, April 2010.

[24] S. Li, Z Teng., and Y. Zhou. Free Vibration of Heated Euler-Bernoulli Beams with Thermal Postbuckling Deformations. *Journal of Thermal Stresses*, 27:843–856, 2004.

[25] M.J. Lighthill. Oscillating Airfoils at High Mach Numbers. *Journal of the Aeronautical Sciences*, 20(6):402–406, June 1953.

[26] S. L. Liguore and G. Tzong. Identification of Knowledge Gaps in the Predictive Capability for Response and Life Prediction of Hypersonic Vehicle Structures. AIAA Paper 2011-1961, April 2011.

[27] S. N. Lophaven, H. B. Nielsen, and J. Sondergaard. DACE A Matlab Kriging Toolbox Version 2.0. Technical Report IMM-TR-2002-12, August 2002.

[28] D. J. Lucia. *Reduced-Order Modeling for High Speed Flows with Moving Shocks*. Ph.D. Thesis, Air Force Institute of Technology, Wright-Patterson AFB, Ohio, 2001.

[29] D. J. Lucia, P. S. Beran, and W. A. Silva. Reduced-Order Modeling: New Approaches for Computational Physics. *Progress in Aerospace Sciences*, 40:51–117, February 2004.

[30] J. J. McNamara, A. R. Crowell, P. P. Friedmann, B. Glaz, and A. Gogulapti. Approximate Modeling of Unsteady Aerodynamics for Hypersonic Aeroelasticity. *Journal of Aircraft*, 47(6):1932–1945, November 2010.

[31] C. Mei, K. Abdel-Motagaly, and R. Chen. Review of Nonlinear Panel Flutter at Supersonic and Hypersonic Speeds. *Applied Mechanics Review*, 52(10):321–332, October 1999.

[32] F. R. Menter and C. L. Rumsey. Assessment of Two-Equation Turbulence Models for Transonic Flows. AIAA Paper 1994-2343, June 1994.

[33] MIL-HDBK-5J. Metallic Materials and Elements for Aerospace Vehicle Structures. Department of Defense, January 2003.

[34] D. E. Myers, C. J. Martin, and M. L. Blosser. Parametric Weight Comparison of Advanced Metallic, Ceramic Tile, and Ceramic Blanket Thermal Protection Systems. NASA TM 2000-210289, June 2000.

[35] I. Nydick, P. P. Friedmann, and X. Zhong. Hypersonic Panel Flutter Studies on Curved Panels. AIAA Paper 1995-1485, April 1995.

[36] J. Park and J. Kim. Thermal Postbuckling and Vibration Analyses of Functionally Graded Plates. *Journal of Sound and Vibration*, 289:77–93, 2006.

[37] N. V. Queipo, R. T. Haftka, W. Shyy, T. Goel, R. Vaidyanathan, and P. K. Tucker. Surrogate-Based Analysis and Optimization. *Progress in Aerospace Sciences*, 41:1–28, January 2005.

[38] C. J. Riley and F. R. DeJarnette. Engineering Aerodymanic Heating Method for Hypersonic Flow. *Journal of Spacecraft and Rockets*, 29(3):327–334, May–June 1992.

[39] C. J. Roy and F. G. Blottner. Methodology for Turbulence Model Validation: Application to Hypersonic Flows. *Journal of Spacecraft and Rockets*, 40(3):313–325, May–June 2003.

[40] C. L. Rumsey. Compressibility Considerations for k-w Turbulence Models in Hypersonic Boundary Layer Applications. NASA/TM-2009-215705, April 2009.

[41] J. Sacks, W. J. Welch, T. J. Mitchell, and H. P. Wynn. Design and Analysis of Computer Experiments. *Statistical Science*, 4(4):409–435, 1989.

[42] W. A. Silva. Identification of Nonlinear Aeroelastic Systems Based on the Volterra Theory: Progress and Opportunities. *Nonlinear Dynamics*, 39(1–2):25–62, January 2005.

[43] S. Suresh, S. N. Omkar, V. Mani, and T. N. Guru Prakash. Lift Coefficient Prediction at High Angle of Attack Using a Recurrent Neural Network. *Aerospace Science and Technology*, 7(1):595–602, 2003.

[44] L. Tang, P. Chen, D. Liu, X. Gao, W. Shyy, Y. Utturkar, and B. Zhang. Proper Orthogonal Decomposition and Response Surface Method for TPS/RLV Structural Design and Optimization: X-43 Case Study. AIAA Paper 2005-839, January 2005.

[45] M. E. Tauber. A Review of High-Speed, Convective, Heat-Transfer Computation Methods. NASA TP-2914, 1989.

[46] P. C. Trizila, C. Kang, M. R. Visbal, and W. Shyy. A Surrogate Model Approach in 2D Versus 3D Flapping Wing Aerodynamic Analysis. AIAA Paper 2008-5914, 2008.

[47] E. V. Zoby and R. A. Graves, Jr. Comparison of Turbulent Prediction Methods with Ground and Flight Test Heating Data. *AIAA Journal*, 15(7):901–902, July 1977.

[48] E. V. Zoby, J. N. Moss, and K. Sutton. Approximate Convective-Heating Equations for Hypersonic Flows. *Journal of Spacecraft and Rockets*, 18(1):64–70, January–February 1981.

[49] B. Zuchowski, S. J. Macquire, and P. McAuliffe. Investigation of Shortfalls in Hypersonic Vehicle Structure Combined Environment Analysis Capability. AIAA Paper 2011-2013, April 2011.